

## An updated model for the Perseus Spiral Arm from Trigonometric Parallax and 3D kinematic distances of distant young stars

L. J. HYLAND,<sup>1,2</sup> M. J. REID,<sup>3</sup> S. P. ELLINGSEN,<sup>2</sup> A. BRUNTHALER,<sup>4</sup> X. W. ZHENG,<sup>5</sup> AND K. M. MENTEN<sup>‡4</sup>

<sup>1</sup>*School of Natural Sciences, University of Tasmania, Private Bag 37, Hobart, Tasmania 7001, Australia*

<sup>2</sup>*International Centre for Radio Astronomy Research, The University of Western Australia, 35 Stirling Highway, Crawley WA 6009, Australia*

<sup>3</sup>*Center for Astrophysics | Harvard and Smithsonian, 60 Garden Street, Cambridge, MA 02138, USA*

<sup>4</sup>*Max-Planck-Institut für Radioastronomie, Auf dem Hügel 69, 53121 Bonn, Germany*

<sup>5</sup>*Nanjing University, Nanjing 20093, China*

Submitted to ApJ

### ABSTRACT

We report trigonometric parallaxes and proper motions for three water masers and one methanol maser obtained with the VLBA as part of the BeSSeL Survey. Incorporating these parallaxes with 3-dimensional kinematic distances, we find the Perseus spiral arm in the 1<sup>st</sup> Galactic quadrant to lie between 0.5 and 1.0 kpc further from the Galactic Center than previously determined. Based on these results, the Perseus and Sagittarius arms intersect at a Galactocentric azimuth of  $189^{+31}_{-19}$  and radius of  $5.6^{+0.3}_{-0.4}$  kpc on the far side of the Galaxy.

### 1. INTRODUCTION

We are still refining our understanding of the size and structure of the Milky Way. The Bar and Spiral Structure Legacy (BeSSeL) Survey (Brunthaler et al. 2011; Reid et al. 2009, 2014, 2019), and the VLBI Exploration of Radio Astrometry (VERA; Honma et al. 2012; VERA Collaboration et al. 2020) project have measured over 250 parallaxes to masers associated with high-mass star-forming regions. These measurements locate spiral arms in the 1<sup>st</sup>, 2<sup>nd</sup> and 3<sup>rd</sup> Galactic quadrants out to a distance from the Sun of  $\approx 10$  kpc. Observations by Southern Hemisphere Parallax Interferometric Radio Astrometry Legacy Survey (S $\pi$ RALS; Hyland et al. 2023) are now providing parallaxes in the 4<sup>th</sup> quadrant with distances expected up to 10 kpc (Hyland et al. 2025). The final frontier of Galactic VLBI astrometry is to measure accurate distances to sources located on the far side of the Milky Way and through these improve our knowledge of the associated spiral arms and other structures.

Corresponding author: Lucas Jordan Hyland  
Lucas.Hyland@utas.edu.au

<sup>‡</sup> Sadly, Prof Karl M. Menten passed away before the publication of this manuscript

The Perseus spiral arm has long been considered one of the major arms of the Milky Way (e.g., Georgelin & Georgelin 1976), but its structure in distant regions past the Galactic center remains uncertain. Recently, Xu et al. (2023) and Bian et al. (2024) presented evidence that it merges with the Sagittarius-Carina arm is this distant part of the Milky Way. In this paper, we present Very Long Baseline Array (VLBA<sup>1</sup>) astrometric measurements for four astrophysical masers in the 1<sup>st</sup> quadrant of the Perseus arm. Using these new measurements and by incorporating 3-dimensional kinematic distances (3DKD; Reid 2022) we are able to accurately determine distances to these masers and refine previous distances. We model the location and shape of the Perseus spiral arm over nearly its full trace and estimate where it appears to merge with the Sagittarius-Carina arm.

### 2. METHODS

The absolute distance accuracy for maser VLBI trigonometric parallax measurements has been recorded as good as 1.2 pc (to the Pleiades cluster at 136.2 pc; Melis et al. 2014), however, due to the inverse rela-

<sup>1</sup> The VLBA is operated by the National Radio Astronomy Observatory. The National Radio Astronomy Observatory is a facility of the National Science Foundation operated under cooperative agreement by Associated Universities, Inc.

tionship between parallax and distance  $\pi = \frac{1}{d}$ , distant sources have a much poorer absolute accuracies ( $\sigma_d = \frac{\sigma_\pi}{\pi^2}$ ) and are subject to a bias from an asymmetric probability distribution, making the determination of distant portions of the spiral arms difficult.

Standard kinematic distances are subject to significant issues, namely, for Galactic radii ( $R$ ) smaller than the Sun’s Galactic radius ( $R_0$ ), there are two distances that have the same  $v_{\text{lsr}}$ . This can also be considered probabilistically - the measured velocity (with uncertainty) in the inner Galaxy will lead to two equal peaks in the distance probability distribution function (PDF). Additional measurements can be used to select which peak is more likely, for example, by incorporating proper motions (Sofue 2011).

Proper motions are the relative angular movement of the target with respect to the Sun, tangential to the line of sight. Scaling proper motions by distance gives velocities, e.g., in Galactic longitude  $v_{l*} = 4.74 d \mu_{l*}$ , where  $v_{l*}$  is in  $\text{km s}^{-1}$   $d$  is distance in kpc and  $\mu_{l*}$  is the proper motion in  $\text{mas yr}^{-1}$ . Using the rotation curve to calculate the component of velocity in the longitude direction, one can estimate a second distance PDF, improving upon the  $v_{\text{lsr}}$  kinematic distance and resolving ambiguities. Given a line of sight ( $l, b$ ) (where  $l$  is the Galactic longitude,  $b$  is the Galactic latitude) an adopted Galactic rotation curve, and measurements of the line-of-sight velocity  $v_{\text{lsr}}$  and transverse proper motions  $\mu_{l*}$  and  $\mu_b$ , the 3DKD method uses these kinematic constraints to build a set of likelihoods from which the most likely distance is inferred Reid (2022).

A key point is that, while the distance uncertainty of trigonometric parallaxes inflates with distance, 3DKD uncertainty is consistent at approximately 1.5 kpc for the current VLBA data (for  $d > 5$  kpc, see Reid 2022). The primary limitations are how well the Milky Way rotation curve is known (uncertainty  $< 5 \text{ km s}^{-1}$  for  $R > 5$  kpc), and maser source non-circular motions ( $\approx 7 \text{ km s}^{-1}$  per coordinate; Reid et al. 2019). In practice, with current VLBA astrometric capabilities, trigonometric parallaxes generally yield more accurate distance estimates for sources  $\lesssim 8$  kpc from the Sun, while 3D kinematic distances are often more accurate for more distant sources (Yamauchi et al. 2016; Reid 2022; Bian et al. 2024). By incorporating both 3DKD and parallax, we can more accurately determine distances.

### 3. OBSERVATIONS AND CALIBRATION

We conducted astrometric observations for three 22 GHz water masers, G021.87+00.01 (G021), G037.81+00.41 (G037), and G070.29+01.60 (G070), and one 6.7 GHz methanol maser, G060.57-00.18

(G060), with the VLBA between 2016-2017<sup>2</sup>. The targets and their respective calibrators are listed in Table 1. Each of the selected targets was a candidate for Perseus arm membership based on ( $l, b, v$ ) values.

The data were collected as part of the BeSSeL Survey BR210 program, and the data are accessible and downloadable from the NRAO archive. This program included many masers thought to be distant, and were each observed in three seasons of 4-8-4 epochs respectively, sampled near the Right Ascension peaks of the parallax curve. Each season was separated by 6 months, and epochs within each season were separated by 1-2 week for the middle season, and 3-4 weeks for the other two. Within each epoch, target masers and quasars were observed in a nodding phase referencing mode, with a switching time of 30 seconds.

The telescope baseband data were correlated with the DiFX software correlator (Deller et al. 2011) at Socorro, New Mexico, and reduced in NRAO AIPS (Greisen 2003) and ParselTongue (Kettenis et al. 2006) using a now-standardized VLBI astrometry process. As this has been discussed in many other BeSSeL publications, we will omit the details but refer the reader to Reid et al. (2009).

In each epoch, the final products from this reduction are amplitude- and delay-calibrated visibilities, which have been phase referenced from each of the quasars to the maser, or from a single maser channel to both quasars (inverse phase reference). This subtracts the time-variable atmospheric phase along the line of sight (Alef 1989; Beasley & Conway 1995), leaving the relative position difference to be measured in the resulting synthesized images. If the quasars are used as the phase reference, the maser (normally a single channel/spot) will be located at  $(x_m, y_m)$ <sup>3</sup> relative to the phase center of the image. If the maser is the reference, each quasar will be located at  $(-x_m, -y_m)$ .

For the 6.7 GHz methanol maser G060, we used inverse phase referencing to image each of the two quasar calibrators in all 16 epochs. For the water masers: G021 could only be referenced against a single quasar (as the other quasar was too weak in every epoch), in 8 of 16 epochs due to maser variability; G037 was referenced against both quasars in all 16 epochs, and G070 was referenced against both quasars in 16 and 14 epochs, respectively (Figure 1). The measured positions at each epoch for each maser are included in the (or will be included?) online supplementary material.

<sup>2</sup> Exact dates can be found here: <http://bessel.vlbi-astrometry.org/observations>

<sup>3</sup>  $x = \Delta\alpha \cos \delta, y = \Delta\delta$

**Table 1.** Information on observed masers and quasars. Columns: (1) Name in Galactic coordinates for masers and J2000 for quasars, (2) Right Ascension in J2000, (3) Declination in J2000, (4) average flux density - in self-calibrated images, integrated over the emission region for quasars, in spectrum for masers, (5) separation between maser and quasar, (6) LSR velocity, (7) maser type- either 22 GHz H<sub>2</sub>O or 6.7 GHz class II CH<sub>3</sub>OH, (8) reference for maser discovery 1: [Genzel & Downes \(1979\)](#), 2: [Codella et al. \(1995\)](#), 3: [Szymczak et al. \(2000\)](#), 4: [Genzel & Downes \(1977\)](#).

Name	$\alpha_{\text{J2000}}$ (h m s)	$\delta_{\text{J2000}}$ (d m s)	$S$ (mJy)	$\theta_{\text{sep}}$ (deg)	$v_{\text{lsr}}$ (km s <sup>-1</sup> )	Type	Ref
G021.87+00.01	18 31 01.7367	-09 49 01.116	$\lesssim 1000$	...	+19.6	H <sub>2</sub> O	1
J1825-0737	18 25 37.6096	-07 37 30.013	120	2.566	...		
J1835-1115	18 35 19.5754	-11 15 59.326	< 10	1.793	...		
G037.81+00.41	18 58 53.8794	+04 32 15.004	$\approx 15000$	...	+19.0	H <sub>2</sub> O	2
J1855+0251	18 55 35.4364	+02 51 19.563	70	1.874	...		
J1856+0610	18 56 31.8388	+06 10 16.765	150	1.738	...		
G060.57-00.18	19 45 52.5019	+24 17 42.749	$\approx 5000$	...	+3.7	CH <sub>3</sub> OH	3
J1946+2418	19 46 19.9607	+24 18 56.909	25	0.116	...		
J1949+2421	19 49 33.1420	+24 21 18.245	125	0.921	...		
G070.29+01.60	20 01 45.3486	+33 32 45.711	$\approx 1000$	...	-26.7	H <sub>2</sub> O	4
J1957+3338	19 57 40.5499	+33 38 27.943	125	1.024	...		
J2001+3323	20 01 42.2090	+33 23 44.765	135	0.151	...		

#### 4. ANALYSIS

##### 4.1. Trigonometric Parallax and Proper Motion

We modeled the measured positions  $(x_m, y_m)$  as a function of time using a least-squares fit that simultaneously solves for the trigonometric parallax ( $\pi$ ), proper motions in the East-West ( $\mu_x$ ) and North-South ( $\mu_y$ ) direction, and position offsets near the center of the data  $(x_0, y_0)$  (following [Reid et al. 2009](#)). The parallax signature was computed using Earth-Sun vectors from the NOVAS astrometric routines ([Kaplan et al. 1989](#)). The fits are shown in Figure 1, with the results tabulated in Table 2.

There were insufficient data to measure an accurate trigonometric parallax for G021, as there were no persistent maser spots to track the motion over the full year, and there were no maser detections in the final four epochs. The primary consequence of this is that the trigonometric parallax and  $\mu_x$  proper motion parameters become strongly correlated in the model fit, resulting in poorly constrained estimates for both quantities. To break this degeneracy, we first fit the data for  $(\pi, \mu_x, \mu_y)$ , then use the proper motions (and recession velocity) to calculate a 3D kinematic distance ( $D_{3\text{Dk}}$ , as described in Section 4.3). We then re-fit  $(\mu_x, \mu_y)$ , with  $\pi$  fixed at  $1/D_{3\text{Dk}} = 0.073$  mas. A subsequent iteration produced no significant change in the fitted parameters, indicating convergence. Both the “raw” results and final 3D kinematic-dependent results are presented in Table 2.

We present  $x, y$  proper motions in Table 2 with their formal uncertainties for the maser spots as determined

by the fitting process. However, we ultimately want the proper motion and  $v_{\text{lsr}}$  of the central exciting star for Galactic kinematics, which can differ from that measured for a given maser spot owing to internal source motions. First, we look for a peak in the CO (i.e., from [Dame et al. 2001](#)) that we can assign as the likely bulk recession velocity of the molecular cloud, and use that as  $v_{\text{lsr}}$  moving forwards.

Methanol masers are known to have a relatively low relative velocity compared to the star ([Moscadelli et al. 2010](#)), and generally have a velocity range  $< 15$  km s<sup>-1</sup> ([Green et al. 2017](#)). G060 has only a single maser spot, so we conservatively add 5 km s<sup>-1</sup> (which, at the measured distance of 7.7 kpc, gives 0.13 mas yr<sup>-1</sup>) in quadrature to the proper motion and  $v_{\text{lsr}}$  uncertainty for G060. Our water masers G021, G037, and G070 have  $v_{\text{lsr}}$  ranges of 6, 10, and 20 km s<sup>-1</sup> respectively and we add 10 km s<sup>-1</sup> in quadrature to the proper motion uncertainty. These values and uncertainties are given in Table 4.

Finally, we rotated the proper motions from R.A/DEC into the Galactic reference frame  $\mu_x, \mu_y \rightarrow \mu_{l*}, \mu_b$ .

##### 4.2. Perseus arm candidate masers

Beginning with the list of all known masers with parallaxes and/or proper motions ([Reid et al. 2019](#); [VERA Collaboration et al. 2020](#), and references therein), we searched for masers associated with the Perseus arm. For  $l > 10^\circ$ , we were able to match maser positions to the expected  $l, v$  trace known from CO measurements ([Reid et al. 2016](#)), without relying on any of the aforementioned astrometric information. This gave a list of

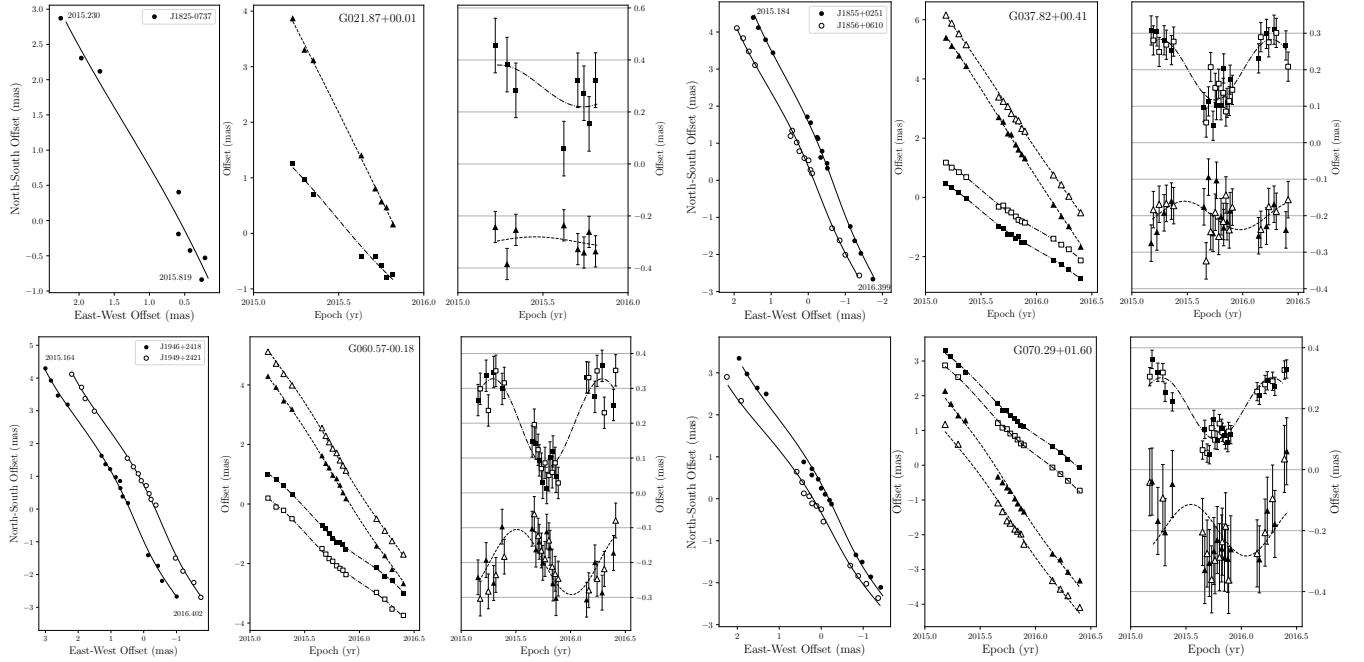


**Figure 1.** Parallaxes and proper motion fits for G021.87+00.01, G037.82+00.41, G060.57-00.18, and G070.29+01.60. Filled and open symbols represent motion with respect to different reference quasars. **Left panels:** Total sky motion, the y-axis is North-South offsets, and the x-axis is East-West offsets. **Center panels:** Time-varying positions in North-South (triangles) and East-West (squares) directions vs. time. The x-axis is time in years, the y-axis is the offset in the corresponding direction. **Right panels:** Proper motion-subtracted time-varying positions in aforementioned directions. For clarity, RA and declination signatures for each reference quasar have been offset from one another.

**Table 2.** Measured parallax and proper motions of masers. **(1)** Maser name, **(2)** quasar name, **(3)** measured parallax, **(4)** measured proper motion in East-West direction, **(5)** measured proper motion in North-South direction. Sources used as the reference in each case are indicated with \*. Uncertainties are given as  $\pm 1\sigma$  for parallaxes and proper motions. *Var-wgt avg* is the variance-weighted average of the previous two rows.

Maser Name	Reference Quasar	Parallax (mas)	$\mu_x$ (mas yr $^{-1}$ )	$\mu_y$ (mas yr $^{-1}$ )
G021.87+00.01	J1825 - 0737*	$0.177 \pm 0.167$	$-2.79 \pm 0.69$	$-6.10 \pm 0.12$
	Using 3D kin	$0.073 \pm 0.006$	$-3.17 \pm 0.17$	$-6.14 \pm 0.09$
G037.82+00.41	J1855 + 0251*	$0.093 \pm 0.010$	$-2.622 \pm 0.025$	$-5.837 \pm 0.036$
	J1856 + 0610*	$0.074 \pm 0.011$	$-2.660 \pm 0.028$	$-5.514 \pm 0.037$
	<i>Var-wgt avg</i>	$0.084 \pm 0.007$	$-2.639 \pm 0.019$	$-5.680 \pm 0.025$
G060.57-00.18*	J1946 + 2418	$0.130 \pm 0.011$	$-3.237 \pm 0.028$	$-5.729 \pm 0.040$
	J1949 + 2421	$0.131 \pm 0.014$	$-3.217 \pm 0.036$	$-5.638 \pm 0.033$
	<i>Var-wgt avg</i>	$0.130 \pm 0.009$	$-3.229 \pm 0.022$	$-5.675 \pm 0.025$
G070.29+01.60	J1957 + 3338*	$0.099 \pm 0.013$	$-2.748 \pm 0.032$	$-4.566 \pm 0.078$
	J2001 + 3323*	$0.109 \pm 0.011$	$-2.984 \pm 0.029$	$-4.394 \pm 0.093$
	<i>Var-wgt avg</i>	$0.104 \pm 0.008$	$-2.877 \pm 0.021$	$-4.444 \pm 0.042$

masers similar to those discussed in (and primarily from) Choi et al. (2014); Reid et al. (2019); Sakai et al. (2019, 2022); Zhang et al. (2013, 2019). For masers within  $l \leq 10^\circ$ , where many spiral arm traces coincide in  $l-v$  space, we used the astrometric measurements to calculate most likely distances (see Section 4.3), and identified one more Perseus candidate maser G001.00-00.23

(Reid et al. 2019). Two other masers, G229.57+00.15 and G240.31+00.07 (Choi et al. 2014), which were previously considered as part of the arm, are a little more ambiguous. We will include G229.57, as it has a  $v_{\text{lsr}}$  consistent with the Perseus arm ( $v_{\text{lsr}} = -53 \pm 10 \text{ km s}^{-1}$ ), and exclude G240.31, as it does not ( $v_{\text{lsr}} = -68 \pm 10 \text{ km s}^{-1}$ ).

This gave 47 candidate masers (see Table 4).

### 4.3. Distance determination

Using the astrometric  $(l, b, \pi)$  and kinematic  $(v, \mu_{l*}, \mu_b)$  parameters, we constructed PDFs for distance:  $P_\pi$  from parallax,  $P_{v_{\text{lsr}}}$  from Doppler velocity,  $P_{\mu_{l*}}$  from longitude motion, and  $P_{\mu_b}$  from latitude motion. We include a brief description of the process in the Appendix. Due to potential non-circular motions and as the non-parallax PDFs rely on models rather than direct measurement alone, to be conservative, we allow for possible systematics by adding a small constant probability density (of  $0.0005 \text{ kpc}^{-1}$ ) to each  $0.025 \text{ kpc}$  bin of those PDFs.

The parallax distance is estimated by finding the median of  $P_\pi$ ,  $d = 1/p$ . The 3DKD is determined via the method of Reid (2022) - multiplying the  $P_{v_{\text{lsr}}}, P_{\mu_{l*}}, P_{\mu_b}$  PDFs and searching for a peak in the new PDF ( $P_{3\text{DKD}}$ ). Finally, by multiplying  $P_\pi$  and  $P_{3\text{DKD}}$ , the peak of the resulting PDF ( $P_{\text{ML}}$ ) is what we consider to be the most likely distance ( $D_{\text{ML}}$ ) that would lead to the measurement of  $\pi, v_{\text{lsr}}, \mu_x, \mu_y$ . Figure 2 gives a graphical example of this process.

Many of the PDFs we are dealing with are asymmetric, multi-peaked, or otherwise non-Gaussian. We therefore estimate uncertainties by determining the smallest contiguous interval in distance that contains 68% of the total integrated probability. The bounds of this interval are quoted as the lower and upper uncertainties on the peak value in Table 4.

Bian et al. (2024) calculate final distances by taking the variance-weighted average of the parallax and 3DKD, where the uncertainty is the inverse square root sum of the weights. Although this does not account for asymmetric PDFs and may underestimate the uncertainties in those cases, their approach will mostly give similar results since the vast majority of parallaxes have less than 15% uncertainties.

Many masers in the 2<sup>nd</sup> Galactic quadrant, exhibit non-circular motions exceeding  $20 \text{ km s}^{-1}$  (Sakai et al. 2019). This leads to anomalous kinematic distances (Xu et al. 2006); consequently, we do not incorporate standard or 3D kinematic distance estimates (relying instead on purely the parallaxes) for seven masers<sup>4</sup>, to avoid introducing a known additional systematic error.

In Figure 3 we compare a map of the Perseus arm sources generated purely from parallax measurements versus combining parallax and 3DKD information as described above. The latter method appears to naturally ‘tighten up’ the distribution of distance points, resulting

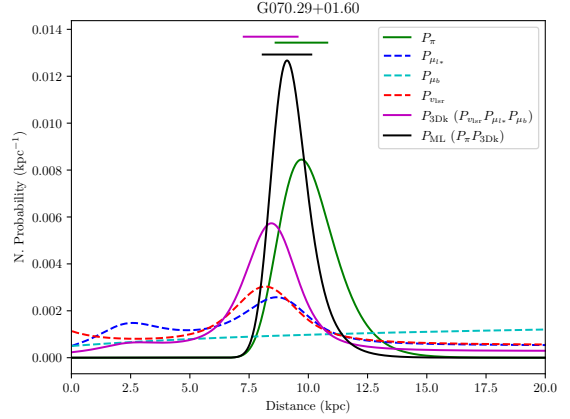


**Figure 2.** Example of the distance determination process for G070.29+01.60. The  $v_{\text{lsr}}$  PDF (dashed-red) and  $l_*, b$  (dashed-blue, cyan) proper motion PDFs are multiplied together to give the 3D kinematic distance PDF (magenta). This is then multiplied by the parallax PDF (green) to give the final PDF (black), the peak of which gives the most likely distance.

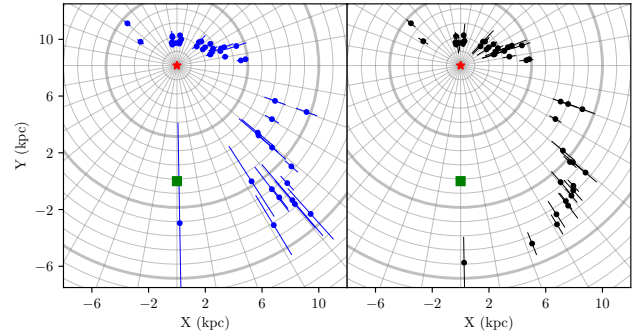


**Figure 3.** Comparison of parallax distance (left, blue dots) with most likely distance (right, black dots) in the Galactic polar coordinate ‘plan view’ frame. With no spiral structure/arm position *a priori*, maser positions converge to a much cleaner spiral shape. We have excluded G021.87 and G070.33 from the parallax distance plot as they do not have a well-measured parallax. The thin concentric rings centered on the Sun (red star at  $[0, 8.15]$ ) are spaced by 1 kpc, and the thick concentric circles are spaced by 5 kpc. The rays show Galactic longitude, spaced by 10 deg. The green square shows the location of the Galactic center at  $[0, 0]$  in both plots.

in a more visually obvious arm, and ultimately an arm fit with lower uncertainty. It is worth reiterating that no prior was used that characterizes the position or shape of the Perseus arm, and that the convergence of distances into a clear spiral arm shape arises by purely considering the astrometric measurements and the model for the Galactic rotation curve.

<sup>4</sup> G108.42+00.89, G108.47-02.81, G108.59+00.49, G111.54+00.77, G122.01-07.08, G133.94+01.06, and G134.62-02.19

Model	$\beta_k$ (deg)	$R_k$ (kpc)	$\psi_<$ (deg)	$\psi_>$ (deg)	width (kpc)
Two segment (Reid et al. 2019)	40	$8.87 \pm 0.13$	$10.3 \pm 1.4$	$8.7 \pm 2.7$	$0.35 \pm 0.06$
Two segment (this work)	40	$9.29 \pm 0.10$	$5.9 \pm 1.2$	$10.6 \pm 1.0$	$0.32 \pm 0.04$
One segment (this work)	40	$9.08 \pm 0.08$	$8.76 \pm 0.72$		$0.36 \pm 0.06$

**Table 3.** Perseus arm fitting results. Columns are (1) model, (2) kink Galactic azimuth in deg, (3) kink Galactic radius in kpc, (4) pre-kink and (5) post-kink pitch angle in deg, (6) arm width in kpc. For the single segment fit, have populated both pitch angle columns with the single fitted pitch angle.

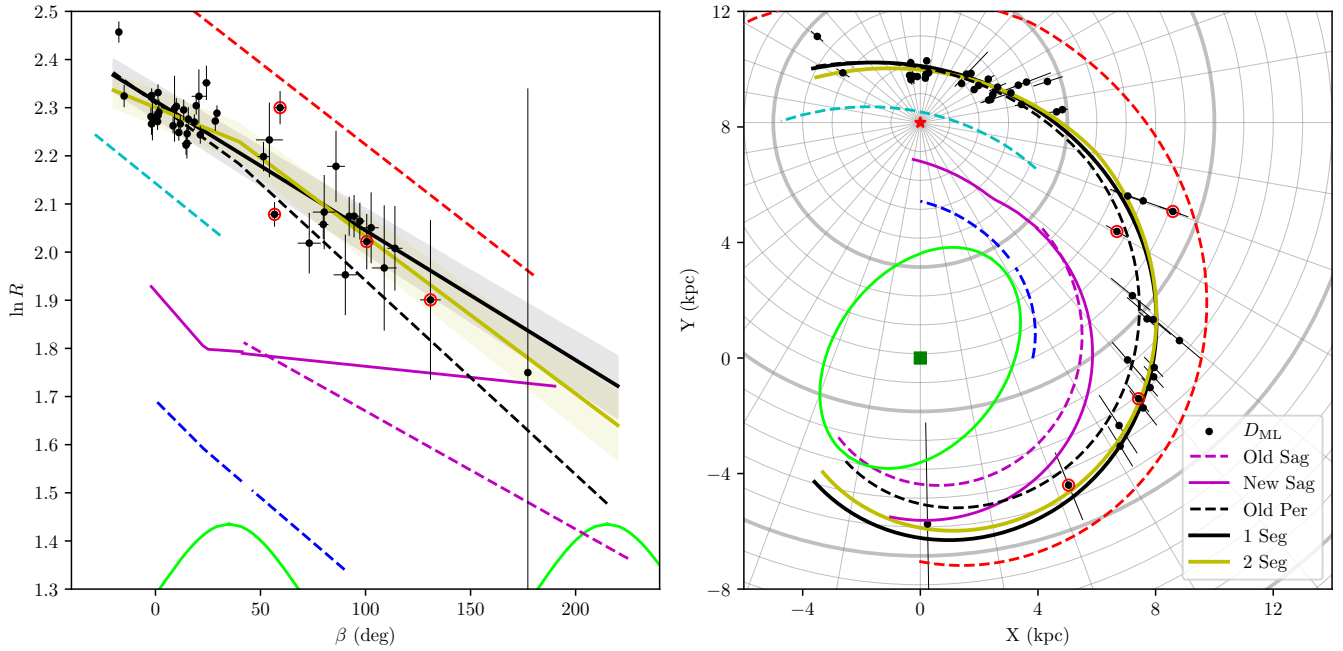


**Figure 4.** **Left:** The log-periodic spiral arm fits. The shaded area shows the estimated Perseus arm width. **Right:** Plan view of the Milky Way. In both plots, the dashed lines are the spiral arm fits for the Outer (red), Perseus (black), Local (cyan), Sagittarian-Carina (magenta), and Scutum-Centaurus (blue) arms (Reid et al. 2019). The solid lines show the new models from this work (black), the Sagittarius fit (magenta; Bian et al. 2024), and X1 bar orbitals (lime; Kumar et al. 2025). The “K” shows the location of the Perseus arm kink, the green square shows the location of the Galactic center  $[0, 0]$ , the Sun is shown with a red star at  $[0, 8.15]$ , and new maser parallaxes from this work are highlighted with red circles.

#### 4.4. Spiral arm fitting

Using the measured  $(l, b, D_{\text{ML}})$  values for each maser, we project the position of each source onto the Galactic plane as in Figure 3. In order to fit spiral arm segments to these data we use a polar Galactic coordinate system  $(R, \beta)$ , where  $R$  is the Galactic radius and  $\beta$  is the Galactic azimuth increasing clockwise from the Sun. This requires a distance to the Galactic center  $R_0$ , which we adopt to be  $R_0 = 8.15$  kpc (Reid et al. 2019). The method to convert  $(l, b, D_{\text{ML}}) \rightarrow (R, \beta)$ , is given in the Appendix. We will model the spiral arm as log-periodic with optional ‘‘kinks’’ (Reid et al. 2019):

$$\ln R = \ln R_k - (\beta - \beta_k) \tan \psi \quad (1)$$

The pitch angle  $\psi$  is allowed to have different values pre- and post-kink position  $(\beta_k, \ln R_k)$ ;  $\psi = \psi_<$  if  $\beta < \beta_k$ ,  $\psi = \psi_>$  if  $\beta > \beta_k$ .

We consider two models:

1. An arm with two segments, allowing for a kink. Since there is a clear gap in the HI/CO data and few maser parallaxes between  $30 < \beta < 50^\circ$  (i.e., the Perseus Gap), we fix the value of  $\beta_k = 40^\circ$ . This also permits a direct comparison with the previous model. For this model we fit four parameters  $(R_k, \psi_<, \psi_>, \text{width})$ .
2. A single arm segment with no kink. We fit for three parameters  $(R_k, \psi, \text{width})$ , where the  $R_k$  is just a reference point on the arm where it goes through  $\beta = 40^\circ$ .

Using a Bayesian Markov Chain Monte Carlo approach described in Reid et al. (2014), we fit for the above parameters, and they are given in Table 3.

## 5. THE PERSEUS ARM

### 5.1. Location and Pitch Angle

We find that the Perseus arm is located further from the Galactic center than previously thought throughout the 1<sup>st</sup> Galactic quadrant, a difference of 0.5 kpc at  $\beta = 40^\circ$  to 1 kpc at  $\beta = 180^\circ$ . Our value for the post-kink pitch angle of  $\psi_> = 10.3 \pm 0.8^\circ$  is slightly larger and more precise than the previous estimate of  $\psi_> = 8.7 \pm 2.7^\circ$ , but consistent within  $1\sigma$ . Our new arm model being further out necessitates a much smaller pre-kink pitch angle of  $\psi_< = 5.8 \pm 0.7^\circ$  compared to the previous value of  $\psi_< = 10.3 \pm 1.4^\circ$ . This is in spite the fact that many of the derived positions for nearby masers remains largely unchanged (see Figure 3), and further highlights G229 as a Perseus arm outlier.

### 5.2. Perseus and Sagittarius arm bifurcation

Xu et al. (2023) propose that the Perseus and Sagittarius spiral arms originate as a single arm on the far side of the Galactic center and then bifurcate in two arms. This is supported by an updated model for the Sagittarius arm by Bian et al. (2024) in which that arm starting at  $\beta \approx 70^\circ$  gradually moves radially outward by about 1 kpc at  $\beta \approx 150^\circ$ , where it would intersect the Perseus arm model of Reid et al. (2019).

Since our results also move the Perseus arm radially outward, we can refine the potential location of a bifurcation. By taking trial models for the Perseus and Sagittarius arms sampled according to their uncertainties and solving for the crossing points, we estimate that the two arms cross at  $\beta = 189^{+31}_{-19}$ ,  $R = 5.6^{+0.3}_{-0.4}$  kpc. It is unclear what form the arms take before this point. If the two arms have a common origin at far side of the Galactic Bar, this parent ‘Perseus-Sagittarius-Carina’ (PSC) arm may extend from the end of the bar at approximately  $\beta = 215^\circ$  (i.e., Kumar et al. 2025). If this is the case, then this short arm segment would require a sharp pitch angle of  $\psi \approx 30^\circ$ . Targeting maser sources in regions between  $l = 340 - 360^\circ$  would be extremely valuable in determining where/if this PSC arm interacts with the long bar.

## 6. SUMMARY

We have conducted astrometric observations towards four masers in high mass star-forming regions in the 1st quadrant of the Milky Way; G021.87+00.01, G037.82+00.41, G060.57-00.18, and G070.29+01.60; and found that all four were in the Perseus spiral arm.

We propose and demonstrate an alternative most likely method to determine the distance to a maser given astrometric and kinematic parameters, which balances the low fractional uncertainty of nearby parallaxes and the relatively distance-invariant uncertainty of 3D kinematic distances.

With these new measurements and our revised distance-determination method, we recalculate distances to previously observed masers and re-evaluate the location and structure of the distant Perseus arm. The updated spatial distribution of masers traces a more coherent spiral pattern, placing the arm between 0.5 and 1 kpc farther from the Galactic Center than in earlier models. In this revised geometry, the Perseus arm intersects the Sagittarius arm at  $\beta = 189^{+31}_{-19}$ , favoring the bifurcation model proposed by Xu et al. (2023). Using the combined dataset, we have now mapped the Perseus arm over its entire length where masers are currently known.

## APPENDIX

## 6.1. Calculating Probability Distribution Functions

Here, we briefly discuss how we create the distance PDFs used in these analyses. Generally, we need to calculate the difference between the measured value and a trial value that depends on the distance. In the case of parallax, the measured value is  $\pi$ , and the model that depends on distance is  $1/d$ , so the difference is  $\Delta\pi = \pi - 1/d$ . We then calculate the likelihood of measuring  $\pi$  if the true distance is  $d$  by using the Gaussian function:

$$P(d) = \frac{d\pi}{dd} P(\pi) \propto \pi^2 e^{-\Delta\pi^2/2\sigma_\pi^2} \quad (2)$$

where  $\sigma_\pi$  is the uncertainty associated with the measurement of  $\pi$ . The differences for LSR velocity, Galactic longitude and latitude proper motion are:

$$\begin{aligned} \Delta v_{\text{lsr}} &= \left( \Theta(R) \frac{R_0}{R} - \Theta_0 \right) \sin l - v_{\text{lsr}} \\ \Delta \mu_{l*} &= \frac{1}{4.74 d} \left( \Theta(R) \cos(l + \beta) - (\Theta_0 + V_0) \cos l + U_0 \sin l \right) \\ &\quad - \mu_{l*} \\ \Delta \mu_b &= \frac{W_0}{4.74 d} - \mu_b \end{aligned}$$

where  $\Theta(R)$  is a rotation curve at Galactic radius  $R$ ,  $\Theta_0$  is the local velocity,  $V_0, U_0, W_0$  are the peculiar motions of the Sun w.r.t  $\Theta_0$  in the Galactic  $X, Y, Z$  directions, and  $\beta$  is the Galactic azimuth (increasing clockwise from the Sun). In order to parameterize in  $d$ , we have:

$$\begin{aligned} R &= \sqrt{R_0^2 + d^2 \cos^2 b - 2R_0 d \cos b \cos l} \\ \beta &= \arctan 2 \left( \frac{d \cos b \sin l}{R}, \frac{R_0 - d \cos b \cos l}{R} \right) \end{aligned}$$

For these analysis, we use the Universal Rotation Curve (Persic et al. 1996) with  $a_1, a_2, a_3, R_0, \Theta_0, V_0, U_0, W_0$  parameters from the A5 fit of Reid et al. (2019).

## 6.2. Notes on individual masers

*G229.57+00.15*: This water maser has a low fractional uncertainty parallax-distance (Choi et al. 2014) that the 3D kinematic distance agrees with. However, its position at 2.6 arm-widths from the center of the Perseus arm puts it midway between the Perseus and Outer arms, and is the most extreme case. There is a bridge of HI at  $l = 230^\circ$  (in the LAB data; Kalberla et al. 2005) connecting what we believe to be the Perseus and Outer arms (Reid et al. 2016), and G229.57 may be associated with that bridge.

*G174.20-00.07 and G183.72-03.66*: As these masers are very close to the Galactic anti-center, and the parallax distances gives result which are very close to us

(Burns et al. 2017; Choi et al. 2014), the recession velocity and proper motions are consistent with zero, and there is very little kinematic information to draw from. As such, a reasonable 3D kinematic distance for this source could not be determined. The parallax has a low fractional uncertainty and dominates the distance determination.

*G070.18+01.74, G070.29+01.60 & G070.32+01.58*: These masers form something akin to a ‘finger of God’, pointing back towards the Sun. They all have a  $v_{\text{lsr}}$  that strongly favors the Perseus arm ( $v \sim -25 \text{ km s}^{-1}$ ) over the Outer arm ( $v \approx -70 \text{ km s}^{-1}$ ). However, both G070.29 (this work) and G070.33 (Sakai et al. 2022) have most likely distances that place them together between the Perseus and Outer arms, with G070.18 being (Zhang et al. 2019). In contrast, the parallax and the 3D kinematic distance for G070.18 share the largest agreement. This could be evidence of a connecting filament between the Perseus and Outer arm at this position.

*G049.41+00.32*: This water maser has a discrepancy between the 3D kinematic distance ( $11.7 \pm 0.8 \text{ kpc}$ ) and the parallax-distance ( $7.6 \pm 1.8 \text{ kpc}$ ; Zhang et al. 2019). The original parallax has a fractional uncertainty of 23%, giving it a skewed parallax PDF. The parallax distance would place it between the Sagittarius and Perseus arms, however the velocity ( $v_{\text{lsr}} = -12 \pm 5 \text{ km s}^{-1}$ ) matches the Perseus arm, so we find that the most likely distance is  $11.6 \pm 0.6 \text{ kpc}$ .

*G040.62-00.13*: This methanol maser has a velocity ( $v_{\text{lsr}} = 31 \pm 5 \text{ km s}^{-1}$ ) that is spurious with the Perseus arm ( $\approx 5 \text{ km s}^{-1}$  for this longitude), and the parallax has a reasonably high fractional uncertainty (20%; Zhang et al. 2019). The longitude proper motion and parallax distance favor  $\approx 12 \text{ kpc}$ , whereas  $v_{\text{lsr}}$  favors  $10.6 \text{ kpc}$ . We exclude  $P_{v_{\text{lsr}}}$  from the  $D_{\text{ML}}$ , giving the most likely distance of  $12.2 \pm 1.2 \text{ kpc}$ . This source may have some significant non-circular motions.

*G021.87+00.01*: The maser spots in this water maser faded in the last season, meaning that the parallax could not be measured directly with these data. The proper motions give a kinematic distance that is consistent with the standard kinematic distance.

*G001.00-00.23*: The original parallax measurement for this source of  $0.09 \pm 0.06 \text{ mas}$  (Reid et al. 2019) places it at a large distance, although with a high fractional uncertainty. The most likely distance places it almost directly in the bifurcation region.

## 6.3. Maser Most Likely Distances

Maser Name	$\pi$ (mas)	$\mu_x$ (mas/yr)	$\mu_y$ (mas/yr)	$v_{lsr}$ (km s <sup>-1</sup> )	$D_\pi$ (kpc)	$D_{3Dk}$ (kpc)	$D_{ML}$ (kpc)	Ref <sup>†</sup>
G001.00-00.23(C)	0.090 ± 0.057	-3.87 ± 0.28	-6.23 ± 0.56	+2 ± 5	11.10 <sup>+14</sup> <sub>-4.3</sub>	13.93 <sup>+1.9</sup> <sub>-1.9</sub>	13.85 <sup>+1.8</sup> <sub>-1.9</sub>	24
G021.87+00.01(H)	0.174 ± 0.126	-3.17 ± 0.48	-6.13 ± 0.21	+19 ± 10	5.75 <sup>+15</sup> <sub>-2.4</sub>	13.55 <sup>+0.82</sup> <sub>-0.80</sub>	13.53 <sup>+0.82</sup> <sub>-0.80</sub>	1
G031.24-00.11(H)	0.076 ± 0.014	-2.80 ± 0.19	-5.54 ± 0.19	+24 ± 10	13.15 <sup>+3.</sup> <sub>-2.0</sub>	13.10 <sup>+0.97</sup> <sub>-0.85</sub>	13.10 <sup>+0.90</sup> <sub>-0.78</sub>	2
G032.79+00.19(H)	0.103 ± 0.031	-2.94 ± 0.24	-6.07 ± 0.25	+16 ± 10	9.70 <sup>+4</sup> <sub>-2.2</sub>	12.55 <sup>+0.78</sup> <sub>-0.78</sub>	12.48 <sup>+0.75</sup> <sub>-0.80</sub>	2
G037.49+00.52(H)	0.091 ± 0.016	-2.74 ± 0.27	-5.49 ± 0.22	+11 ± 10	11.00 <sup>+2</sup> <sub>-1.7</sub>	12.55 <sup>+0.80</sup> <sub>-0.75</sub>	12.40 <sup>+0.75</sup> <sub>-0.72</sub>	8
G037.82+00.41(H)	0.085 ± 0.007	-2.68 ± 0.21	-5.60 ± 0.23	+16 ± 10	11.78 <sup>+1</sup> <sub>-0.90</sub>	12.22 <sup>+0.78</sup> <sub>-0.75</sub>	12.05 <sup>+0.62</sup> <sub>-0.57</sub>	1, 8
G040.42+00.70(C)	0.078 ± 0.013	-2.95 ± 0.09	-5.48 ± 0.10	+10 ± 5	12.82 <sup>+2.5</sup> <sub>-1.8</sub>	12.00 <sup>+0.42</sup> <sub>-0.40</sub>	12.05 <sup>+0.40</sup> <sub>-0.40</sub>	2
G040.62-00.13(C)	0.080 ± 0.021	-2.69 ± 0.12	-5.60 ± 0.25	+31 ± 5	12.50 <sup>+4</sup> <sub>-2.6</sub>	10.75 <sup>+0.55</sup> <sub>-0.53</sub>	12.18 <sup>+1.2</sup> <sub>-1.2</sub>	2
G042.03+00.19(C)	0.071 ± 0.012	-2.40 ± 0.09	-5.64 ± 0.11	+12 ± 5	14.07 <sup>+3</sup> <sub>-2.0</sub>	11.75 <sup>+0.47</sup> <sub>-0.45</sub>	11.88 <sup>+0.50</sup> <sub>-0.42</sub>	2
G043.16+00.01(H)	0.088 ± 0.005	-2.48 ± 0.15	-5.27 ± 0.13	+11 ± 5	11.38 <sup>+0.65</sup> <sub>-0.60</sub>	11.65 <sup>+1.1</sup> <sub>-0.62</sub>	11.50 <sup>+0.48</sup> <sub>-0.42</sub>	3
G048.60+00.02(H)	0.093 ± 0.005	-2.89 ± 0.13	-5.50 ± 0.13	+18 ± 5	10.75 <sup>+0.60</sup> <sub>-0.53</sub>	9.90 <sup>+0.53</sup> <sub>-0.53</sub>	10.32 <sup>+0.42</sup> <sub>-0.35</sub>	3
G049.26+00.31(C)	0.113 ± 0.016	-2.73 ± 0.15	-5.85 ± 0.19	+0 ± 5	8.85 <sup>+1.5</sup> <sub>-1.1</sub>	10.68 <sup>+0.57</sup> <sub>-0.55</sub>	10.50 <sup>+0.53</sup> <sub>-0.70</sub>	2
G049.41+00.32(C)	0.132 ± 0.031	-3.15 ± 0.17	-4.49 ± 0.66	-12 ± 5	7.58 <sup>+2</sup> <sub>-1.4</sub>	11.68 <sup>+0.60</sup> <sub>-0.55</sub>	11.58 <sup>+0.55</sup> <sub>-0.58</sub>	2
G050.28-00.39(H)	0.135 ± 0.026	-3.29 ± 0.56	-5.52 ± 0.37	+17 ± 5	7.40 <sup>+1.8</sup> <sub>-1.18</sub>	9.50 <sup>+0.57</sup> <sub>-0.57</sub>	9.35 <sup>+0.55</sup> <sub>-0.65</sub>	9
G060.57-00.18(C)	0.130 ± 0.009	-3.23 ± 0.13	-5.68 ± 0.13	+3 ± 5	7.70 <sup>+0.6</sup> <sub>-0.50</sub>	7.78 <sup>+0.70</sup> <sub>-0.88</sub>	7.72 <sup>+0.42</sup> <sub>-0.42</sub>	1, 24
G070.18+01.74(C)	0.136 ± 0.014	-2.85 ± 0.15	-5.18 ± 0.18	-23 ± 5	7.35 <sup>+0.8</sup> <sub>-0.68</sub>	7.70 <sup>+0.65</sup> <sub>-0.68</sub>	7.55 <sup>+0.53</sup> <sub>-0.50</sub>	2
G070.29+01.60(H)	0.103 ± 0.008	-2.81 ± 0.20	-4.44 ± 0.20	-27 ± 10	9.70 <sup>+0.8</sup> <sub>-0.68</sub>	8.32 <sup>+0.88</sup> <sub>-0.88</sub>	9.20 <sup>+0.60</sup> <sub>-0.50</sub>	1
G070.32+01.58(H)	0.074 ± 0.037	-2.82 ± 0.29	-4.68 ± 0.28	-23 ± 5	13.53 <sup>+11.5</sup> <sub>-4.50</sub>	7.85 <sup>+0.62</sup> <sub>-0.62</sub>	8.08 <sup>+0.60</sup> <sub>-0.58</sub>	9
G094.60-01.79(C,H)	0.221 ± 0.013	-3.49 ± 0.23	-2.65 ± 0.23	-43 ± 5	4.53 <sup>+0.3</sup> <sub>-0.25</sub>	5.28 <sup>+0.62</sup> <sub>-0.65</sub>	4.62 <sup>+0.28</sup> <sub>-0.25</sub>	4, 5
G095.29-00.93(C,H)	0.206 ± 0.007	-2.74 ± 0.30	-2.85 ± 0.37	-38 ± 5	4.85 <sup>+0.2</sup> <sub>-0.15</sub>	4.90 <sup>+0.68</sup> <sub>-0.68</sub>	4.85 <sup>+0.15</sup> <sub>-0.12</sub>	4, 15
G100.37-03.57(H)	0.289 ± 0.016	-3.66 ± 0.60	-3.02 ± 0.60	-37 ± 10	3.45 <sup>+0.2</sup> <sub>-0.15</sub>	4.12 <sup>+1.1</sup> <sub>-1.1</sub>	3.48 <sup>+0.20</sup> <sub>-0.17</sub>	4
G108.20+00.58(H)	0.227 ± 0.037	-2.25 ± 0.50	-1.00 ± 0.50	-49 ± 5	4.40 <sup>+0.9</sup> <sub>-0.60</sub>	4.62 <sup>+0.70</sup> <sub>-0.68</sub>	4.53 <sup>+0.53</sup> <sub>-0.48</sub>	4
G108.42+00.89(H)	0.400 ± 0.050	-2.58 ± 0.60	-1.91 ± 0.50	-51 ± 5	2.50 <sup>+0.4</sup> <sub>-0.28</sub>	4.75 <sup>+0.68</sup> <sub>-0.68</sub>	2.50 <sup>+0.35</sup> <sub>-0.27</sub>	16
G108.47-02.81(H)	0.309 ± 0.010	-3.13 ± 0.49	-2.79 ± 0.46	-54 ± 5	3.23 <sup>+0.1</sup> <sub>-0.07</sub>	4.85 <sup>+0.70</sup> <sub>-0.70</sub>	3.23 <sup>+0.10</sup> <sub>-0.07</sub>	4
G108.59+00.49(H)	0.405 ± 0.033	-5.56 ± 0.40	-3.40 ± 0.40	-52 ± 5	2.48 <sup>+0.2</sup> <sub>-0.17</sub>	0.25 <sup>+3.1</sup> <sub>-0.15</sub>	2.48 <sup>+0.20</sup> <sub>-0.17</sub>	4
G111.23-01.23(H)	0.300 ± 0.081	-4.37 ± 0.60	-2.38 ± 0.60	-53 ± 10	3.33 <sup>+1.</sup> <sub>-0.70</sub>	4.35 <sup>+1.2</sup> <sub>-1.2</sub>	3.82 <sup>+0.98</sup> <sub>-0.87</sub>	4
G111.25-00.76(C,H)	0.280 ± 0.015	-2.69 ± 0.28	-1.75 ± 0.33	-40 ± 3	3.58 <sup>+0.2</sup> <sub>-0.17</sub>	3.67 <sup>+0.53</sup> <sub>-0.53</sub>	3.58 <sup>+0.17</sup> <sub>-0.15</sub>	4, 20
G111.54+00.77(C)	0.378 ± 0.017	-2.45 ± 0.40	-2.44 ± 0.40	-57 ± 5	2.65 <sup>+0.1</sup> <sub>-0.10</sub>	5.00 <sup>+0.70</sup> <sub>-0.70</sub>	2.65 <sup>+0.10</sup> <sub>-0.10</sub>	12
G115.05-00.04(H)	0.356 ± 0.040	-3.70 ± 0.78	-2.00 ± 0.81	-36 ± 5	2.80 <sup>+0.4</sup> <sub>-0.25</sub>	3.15 <sup>+0.62</sup> <sub>-0.62</sub>	2.88 <sup>+0.33</sup> <sub>-0.25</sub>	11
G122.01-07.08(H)	0.460 ± 0.020	-3.70 ± 0.50	-1.25 ± 0.50	-50 ± 5	2.17 <sup>+0.07</sup> <sub>-0.07</sub>	3.95 <sup>+0.75</sup> <sub>-0.75</sub>	2.18 <sup>+0.07</sup> <sub>-0.08</sub>	6
G123.06-06.30(C)	0.421 ± 0.022	-2.69 ± 0.31	-1.77 ± 0.29	-29 ± 3	2.38 <sup>+0.12</sup> <sub>-0.10</sub>	2.40 <sup>+0.47</sup> <sub>-0.47</sub>	2.38 <sup>+0.12</sup> <sub>-0.10</sub>	22
G123.06-06.31(H)	0.355 ± 0.030	-2.79 ± 0.62	-2.14 ± 0.70	-30 ± 5	2.83 <sup>+0.25</sup> <sub>-0.23</sub>	2.52 <sup>+0.60</sup> <sub>-0.60</sub>	2.78 <sup>+0.22</sup> <sub>-0.18</sub>	19
G133.94+01.06(C,H)	0.516 ± 0.008	-1.20 ± 0.32	-0.15 ± 0.32	-45 ± 3	1.95 <sup>+0.03</sup> <sub>-0.03</sub>	3.88 <sup>+0.70</sup> <sub>-0.62</sub>	1.95 <sup>+0.00</sup> <sub>-0.02</sub>	14, 10, 8
G134.62-02.19(H)	0.413 ± 0.017	-0.49 ± 0.50	-1.19 ± 0.48	-39 ± 5	2.42 <sup>+0.10</sup> <sub>-0.07</sub>	3.23 <sup>+0.80</sup> <sub>-0.75</sub>	2.43 <sup>+0.10</sup> <sub>-0.08</sub>	18
G136.84+01.16(C)	0.442 ± 0.123	0.42 ± 0.50	-0.45 ± 0.50	-42 ± 5	2.27 <sup>+0.85</sup> <sub>-0.50</sub>	1.32 <sup>+3.0</sup> <sub>-0.47</sub>	2.05 <sup>+1.55</sup> <sub>-0.40</sub>	20
G170.65-00.24(H)	0.532 ± 0.075	0.23 ± 1.20	-3.14 ± 0.60	-19 ± 5	1.88 <sup>+0.30</sup> <sub>-0.23</sub>	1.23 <sup>+0.47</sup> <sub>-0.45</sub>	1.78 <sup>+0.22</sup> <sub>-0.18</sub>	7
G173.17+02.36(H)	0.590 ± 0.043	0.01 ± 1.20	-3.40 ± 1.20	-10 ± 10	1.70 <sup>+0.12</sup> <sub>-0.10</sub>	1.15 <sup>+0.50</sup> <sub>-0.45</sub>	1.68 <sup>+0.10</sup> <sub>-0.10</sub>	28
G173.48+02.44(C)	0.594 ± 0.014	0.62 ± 0.63	-2.34 ± 0.63	-13 ± 5	1.68 <sup>+0.05</sup> <sub>-0.03</sub>	1.48 <sup>+0.62</sup> <sub>-0.55</sub>	1.68 <sup>+0.03</sup> <sub>-0.02</sub>	20
G173.71+02.69(H)	0.639 ± 0.033	0.79 ± 1.25	-2.41 ± 1.25	-17 ± 10	1.57 <sup>+0.07</sup> <sub>-0.07</sub>	1.38 <sup>+0.70</sup> <sub>-0.55</sub>	1.55 <sup>+0.07</sup> <sub>-0.05</sub>	26
G174.20-00.07(H)	0.467 ± 0.020	0.32 ± 0.56	-0.22 ± 0.68	-2 ± 10	2.15 <sup>+0.07</sup> <sub>-0.07</sub>	11.38 <sup>+13</sup> <sub>-11</sub>	2.15 <sup>+0.08</sup> <sub>-0.07</sub>	25
G183.72-03.66(H)	0.629 ± 0.012	0.38 ± 1.30	-1.32 ± 1.30	+3 ± 5	1.60 <sup>+0.03</sup> <sub>-0.03</sub>	2.65 <sup>+4.2</sup> <sub>-1.6</sub>	1.60 <sup>+0.00</sup> <sub>-0.02</sub>	4
G188.79+01.03(H)	0.496 ± 0.103	-0.10 ± 0.50	-3.91 ± 0.50	+1 ± 5	2.02 <sup>+0.50</sup> <sub>-0.35</sub>	0.80 <sup>+0.33</sup> <sub>-0.35</sub>	1.88 <sup>+0.53</sup> <sub>-0.35</sub>	21
G188.94+00.88(C,H)	0.476 ± 0.006	-0.32 ± 0.49	-1.94 ± 0.49	+8 ± 5	2.10 <sup>+0.03</sup> <sub>-0.03</sub>	1.90 <sup>+0.97</sup> <sub>-0.80</sub>	2.10 <sup>+0.02</sup> <sub>-0.02</sub>	5, 13, 20
G192.16-03.81(C,H)	0.659 ± 0.070	0.69 ± 0.70	-1.57 ± 0.70	+5 ± 5	1.52 <sup>+0.15</sup> <sub>-0.15</sub>	1.43 <sup>+0.8</sup> <sub>-0.65</sub>	1.52 <sup>+0.15</sup> <sub>-0.15</sub>	22, 27
G192.60-00.04(H)	0.601 ± 0.039	-0.18 ± 0.60	-0.43 ± 0.60	+7 ± 5	1.68 <sup>+0.10</sup> <sub>-0.10</sub>	1.77 <sup>+2.8</sup> <sub>-1.6</sub>	1.68 <sup>+0.10</sup> <sub>-0.10</sub>	17
G229.57+00.15(H)	0.218 ± 0.012	-1.33 ± 0.70	0.77 ± 0.70	+53 ± 10	4.58 <sup>+0.28</sup> <sub>-0.23</sub>	4.75 <sup>+2.1</sup> <sub>-1.4</sub>	4.60 <sup>+0.25</sup> <sub>-0.23</sub>	4
G236.81+01.98(H)	0.326 ± 0.026	-2.49 ± 0.43	2.67 ± 0.41	+53 ± 5	3.08 <sup>+0.25</sup> <sub>-0.23</sub>	3.70 <sup>+1.3</sup> <sub>-1.6</sub>	3.10 <sup>+0.25</sup> <sub>-0.23</sub>	4

**Table 4.** Astrometric and kinematic properties of other candidate Perseus arm masers. Columns are: (1) Maser name (type of maser C=methanol, H=water), (2) parallax, (3) proper motion in  $\alpha \cos \delta$ , (4) and  $\delta$  directions, (5) recession velocity, (6) parallax-distance, (7) 3D kinematic distance, (7) most likely distance and, (8) references. When there have been multiple parallaxes measured, we report the variance-weighted parallax in column 3. For the three distance estimates, we report the mode of the probability distribution, and the smallest upper and lower limits that enclose 68% confidence (to account for skewed distributions). †Ref- 1: This work, 2: Zhang et al. (2019), 3: Zhang et al. (2013), 4: Choi et al. (2014), 5: Oh et al. (2010), 6: Moellenbrock et al. (2009), 7: Sakai et al. (2012), 8: Nagayama et al. (2020), 9: Sakai et al. (2022), 10: Matsumoto et al. (2011), 11: Kusuno et al. (2013), 12: Moscadelli et al. (2009), 13: Reid et al. (2009), 14: Xu et al. (2006), 15: Nakanishi et al. (2015), 16: Imai et al. (2012), 17: Shiozaki et al. (2011), 18: Asaki et al. (2010), 19: Sato et al. (2008), 20: Sakai et al. (2019), 21: Niinuma et al. (2011), 22: Rygl et al. (2010), 24: Reid et al. (2019), 25: Burns et al. (2017), 26: Burns et al. (2015), 27: Burns et al. (2016), 28: VERA Collaboration et al. (2020).

## REFERENCES

- Alef, W. 1989, in NATO Advanced Study Institute (ASI) Series C, Vol. 283, Techniques and Applications of Very Long Baseline Interferometry, ed. M. Felli & R. E. Spencer, 261–274, doi: [10.1007/978-94-009-2428-4\\_13](https://doi.org/10.1007/978-94-009-2428-4_13)
- Asaki, Y., Deguchi, S., Imai, H., et al. 2010, *ApJ*, 721, 267, doi: [10.1088/0004-637X/721/1/267](https://doi.org/10.1088/0004-637X/721/1/267)
- Beasley, A. J., & Conway, J. E. 1995, in Astronomical Society of the Pacific Conference Series, Vol. 82, Very Long Baseline Interferometry and the VLBA, ed. J. A. Zensus, P. J. Diamond, & P. J. Napier, 327
- Bian, S. B., Wu, Y. W., Xu, Y., et al. 2024, *AJ*, 167, 267, doi: [10.3847/1538-3881/ad4030](https://doi.org/10.3847/1538-3881/ad4030)
- Brunthaler, A., Reid, M. J., Menten, K. M., et al. 2011, *Astronomische Nachrichten*, 332, 461, doi: [10.1002/asna.201111560](https://doi.org/10.1002/asna.201111560)
- Burns, R. A., Handa, T., Nagayama, T., Sunada, K., & Omodaka, T. 2016, *MNRAS*, 460, 283, doi: [10.1093/mnras/stw958](https://doi.org/10.1093/mnras/stw958)
- Burns, R. A., Imai, H., Handa, T., et al. 2015, *MNRAS*, 453, 3163, doi: [10.1093/mnras/stv1836](https://doi.org/10.1093/mnras/stv1836)
- Burns, R. A., Handa, T., Imai, H., et al. 2017, *MNRAS*, 467, 2367, doi: [10.1093/mnras/stx216](https://doi.org/10.1093/mnras/stx216)
- Choi, Y. K., Hachisuka, K., Reid, M. J., et al. 2014, *ApJ*, 790, 99, doi: [10.1088/0004-637X/790/2/99](https://doi.org/10.1088/0004-637X/790/2/99)
- Codella, C., Palumbo, G. G. C., Pareschi, G., et al. 1995, *MNRAS*, 276, 57, doi: [10.1093/mnras/276.1.57](https://doi.org/10.1093/mnras/276.1.57)
- Dame, T. M., Hartmann, D., & Thaddeus, P. 2001, *ApJ*, 547, 792, doi: [10.1086/318388](https://doi.org/10.1086/318388)
- Deller, A. T., Brisken, W. F., Phillips, C. J., et al. 2011, *PASP*, 123, 275, doi: [10.1086/658907](https://doi.org/10.1086/658907)
- Genzel, R., & Downes, D. 1977, *A&AS*, 30, 145
- . 1979, *A&A*, 72, 234
- Georgelin, Y. M., & Georgelin, Y. P. 1976, *A&A*, 49, 57
- Green, J. A., Breen, S. L., Fuller, G. A., et al. 2017, *MNRAS*, 469, 1383, doi: [10.1093/mnras/stx887](https://doi.org/10.1093/mnras/stx887)
- Greisen, E. W. 2003, in *Astrophysics and Space Science Library*, Vol. 285, Information Handling in Astronomy - Historical Vistas, ed. A. Heck, 109, doi: [10.1007/0-306-48080-8\\_7](https://doi.org/10.1007/0-306-48080-8_7)
- Honma, M., Nagayama, T., Ando, K., et al. 2012, *PASJ*, 64, 136, doi: [10.1093/pasj/64.6.136](https://doi.org/10.1093/pasj/64.6.136)
- Hyland, L. J., Ellingsen, S. P., & Reid, M. J. 2025, arXiv e-prints, arXiv:2510.16998, doi: [10.48550/arXiv.2510.16998](https://doi.org/10.48550/arXiv.2510.16998)
- Hyland, L. J., Reid, M. J., Orosz, G., et al. 2023, *ApJ*, 953, 21, doi: [10.3847/1538-4357/acdbc5](https://doi.org/10.3847/1538-4357/acdbc5)
- Imai, H., Sakai, N., Nakanishi, H., et al. 2012, *PASJ*, 64, 142, doi: [10.1093/pasj/64.6.142](https://doi.org/10.1093/pasj/64.6.142)
- Kalberla, P. M. W., Burton, W. B., Hartmann, D., et al. 2005, *A&A*, 440, 775, doi: [10.1051/0004-6361:20041864](https://doi.org/10.1051/0004-6361:20041864)
- Kaplan, G. H., Hughes, J. A., Seidelmann, P. K., Smith, C. A., & Yallop, B. D. 1989, *AJ*, 97, 1197, doi: [10.1086/115063](https://doi.org/10.1086/115063)
- Kettenis, M., van Langevelde, H. J., Reynolds, C., & Cotton, B. 2006, in *Astronomical Society of the Pacific Conference Series*, Vol. 351, *Astronomical Data Analysis Software and Systems XV*, ed. C. Gabriel, C. Arviset, D. Ponz, & S. Enrique, 497
- Kumar, J., Reid, M. J., Dame, T. M., et al. 2025, *ApJ*, 982, 185, doi: [10.3847/1538-4357/adb70f](https://doi.org/10.3847/1538-4357/adb70f)
- Kusuno, K., Asaki, Y., Imai, H., & Oyama, T. 2013, *ApJ*, 774, 107, doi: [10.1088/0004-637X/774/2/107](https://doi.org/10.1088/0004-637X/774/2/107)
- Matsumoto, N., Honma, M., Isono, Y., et al. 2011, *PASJ*, 63, 1345, doi: [10.1093/pasj/63.6.1345](https://doi.org/10.1093/pasj/63.6.1345)
- Melis, C., Reid, M. J., Mioduszewski, A. J., Stauffer, J. R., & Bower, G. C. 2014, *Science*, 345, 1029, doi: [10.1126/science.1256101](https://doi.org/10.1126/science.1256101)
- Moellenbrock, G. A., Claussen, M. J., & Goss, W. M. 2009, *ApJ*, 694, 192, doi: [10.1088/0004-637X/694/1/192](https://doi.org/10.1088/0004-637X/694/1/192)
- Moscadelli, L., Reid, M. J., Menten, K. M., et al. 2009, *ApJ*, 693, 406, doi: [10.1088/0004-637X/693/1/406](https://doi.org/10.1088/0004-637X/693/1/406)
- Moscadelli, L., Xu, Y., & Chen, X. 2010, *ApJ*, 716, 1356, doi: [10.1088/0004-637X/716/2/1356](https://doi.org/10.1088/0004-637X/716/2/1356)
- Nagayama, T., Kobayashi, H., Hirota, T., et al. 2020, *PASJ*, 72, 52, doi: [10.1093/pasj/psaa034](https://doi.org/10.1093/pasj/psaa034)
- Nakanishi, H., Sakai, N., Kurayama, T., et al. 2015, *PASJ*, 67, 68, doi: [10.1093/pasj/psv012](https://doi.org/10.1093/pasj/psv012)
- Niinuma, K., Nagayama, T., Hirota, T., et al. 2011, *PASJ*, 63, 9, doi: [10.1093/pasj/63.1.9](https://doi.org/10.1093/pasj/63.1.9)
- Oh, C. S., Kobayashi, H., Honma, M., et al. 2010, *PASJ*, 62, 101, doi: [10.1093/pasj/62.1.101](https://doi.org/10.1093/pasj/62.1.101)
- Persic, M., Salucci, P., & Stel, F. 1996, *MNRAS*, 281, 27, doi: [10.1093/mnras/278.1.27](https://doi.org/10.1093/mnras/278.1.27)
- Reid, M. J. 2022, *AJ*, 164, 133, doi: [10.3847/1538-3881/ac80bb](https://doi.org/10.3847/1538-3881/ac80bb)
- Reid, M. J., Dame, T. M., Menten, K. M., & Brunthaler, A. 2016, *ApJ*, 823, 77, doi: [10.3847/0004-637X/823/2/77](https://doi.org/10.3847/0004-637X/823/2/77)
- Reid, M. J., Menten, K. M., Brunthaler, A., et al. 2009, *ApJ*, 693, 397, doi: [10.1088/0004-637X/693/1/397](https://doi.org/10.1088/0004-637X/693/1/397)
- . 2014, *ApJ*, 783, 130, doi: [10.1088/0004-637X/783/2/130](https://doi.org/10.1088/0004-637X/783/2/130)
- . 2019, *ApJ*, 885, 131, doi: [10.3847/1538-4357/ab4a11](https://doi.org/10.3847/1538-4357/ab4a11)
- Rygl, K. L. J., Brunthaler, A., Reid, M. J., et al. 2010, *A&A*, 511, A2, doi: [10.1051/0004-6361/200913135](https://doi.org/10.1051/0004-6361/200913135)
- Sakai, N., Honma, M., Nakanishi, H., et al. 2012, *PASJ*, 64, 108, doi: [10.1093/pasj/64.5.108](https://doi.org/10.1093/pasj/64.5.108)
- Sakai, N., Nakanishi, H., Kurahara, K., et al. 2022, *PASJ*, 74, 209, doi: [10.1093/pasj/psab118](https://doi.org/10.1093/pasj/psab118)

- Sakai, N., Reid, M. J., Menten, K. M., Brunthaler, A., & Dame, T. M. 2019, *ApJ*, 876, 30, doi: [10.3847/1538-4357/ab12e0](https://doi.org/10.3847/1538-4357/ab12e0)
- Sato, M., Hirota, T., Honma, M., et al. 2008, *PASJ*, 60, 975, doi: [10.1093/pasj/60.5.975](https://doi.org/10.1093/pasj/60.5.975)
- Shiozaki, S., Imai, H., Tafuya, D., et al. 2011, *PASJ*, 63, 1219, doi: [10.1093/pasj/63.6.1219](https://doi.org/10.1093/pasj/63.6.1219)
- Sofue, Y. 2011, *PASJ*, 63, 813, doi: [10.1093/pasj/63.4.813](https://doi.org/10.1093/pasj/63.4.813)
- Szymczak, M., Hrynek, G., & Kus, A. J. 2000, *A&AS*, 143, 269, doi: [10.1051/aas:2000334](https://doi.org/10.1051/aas:2000334)
- VERA Collaboration, Hirota, T., Nagayama, T., et al. 2020, *PASJ*, 72, 50, doi: [10.1093/pasj/psaa018](https://doi.org/10.1093/pasj/psaa018)
- Xu, Y., Hao, C. J., Liu, D. J., et al. 2023, *ApJ*, 947, 54, doi: [10.3847/1538-4357/acc45c](https://doi.org/10.3847/1538-4357/acc45c)
- Xu, Y., Reid, M. J., Zheng, X. W., & Menten, K. M. 2006, *Science*, 311, 54, doi: [10.1126/science.1120914](https://doi.org/10.1126/science.1120914)
- Yamauchi, A., Yamashita, K., Honma, M., et al. 2016, *PASJ*, 68, 60, doi: [10.1093/pasj/psw058](https://doi.org/10.1093/pasj/psw058)
- Zhang, B., Reid, M. J., Menten, K. M., et al. 2013, *ApJ*, 775, 79, doi: [10.1088/0004-637X/775/1/79](https://doi.org/10.1088/0004-637X/775/1/79)
- Zhang, B., Reid, M. J., Zhang, L., et al. 2019, *AJ*, 157, 200, doi: [10.3847/1538-3881/ab141d](https://doi.org/10.3847/1538-3881/ab141d)